Reverse-time migration of mobile marine vibrator data

Khalid Almuteri, Paul Sava & Jeffrey Shragge
Center for Wave Phenomena and Dept. of Geophysics, Colorado School of Mines, Golden CO 80401
email kalmuteri@mines.edu

ABSTRACT
Marine vibrators are viable alternatives to seismic air-guns in ocean-bottom acquisition because of their low environmental impact. They are also advantageous due to their ability to generate lower frequency content compared to air-guns, and due to their suitability for simultaneous acquisition. However, mobile marine vibrators introduce a unique set of processing and imaging challenges for ocean-bottom acquisition, such as the Doppler effect and the time-dependent source-receiver offsets, which are not features of conventional marine acquisition. Standard seismic data processing and imaging techniques assume stationary sources and are not fully suitable for mobile marine vibrator data without modification. Not accounting for source motion in seismic imaging introduces phase change and mispositioning of imaged structure. Further, ignoring source motion effects may imply apparent poor illumination, velocity errors, and/or both. Our results show that source motion effects are more severe for shallow targets than deep targets. We propose a reverse-time migration approach that considers the source-motion effects and is capable of producing accurate subsurface images. Synthetic examples illustrate the ability of our proposed method to construct accurate subsurface RTM images even for source velocities higher than what is common in typical marine acquisition. Our approach is not limited to mobile marine vibrator data, but is also applicable to streamer data.

Key words: RTM, marine vibrator, ocean-bottom acquisition

1 INTRODUCTION

Conventional marine impulsive sources (i.e., air-guns) raise concerns over their impact to the environment, renewing an interest in environmentally friendly marine vibrators as viable alternatives. However, marine vibrators are not only attractive for their low environmental impact, but also advantageous from an exploration point of view because they provide data with lower frequencies compared to those acquired using air-guns (Guitton et al., 2021). Further, by blending phase-encoded sources, marine vibrators enable simultaneous acquisition (Laws et al., 2019), reducing acquisition time, which is more challenging to achieve using conventional air-guns (e.g., Wason and Herrmann, 2013). However, marine vibrators are in continuous motion and have a long sweep duration, introducing Doppler effects and time-dependent source-receiver offsets in ocean-bottom acquisition. Therefore, source motion creates new processing and imaging challenges unique to such acquisition scenarios.

Conventional seismic imaging techniques assume stationary sources or negligible source motion. One such technique is reverse-time migration (RTM) (Baysal et al., 1983; McMechan, 1983; Whitmore, 1983). The concept of RTM follows the Claerbout (1971) imaging principle: a reflector exists at a point (x, y, z) in space where a forward propagating source wavefield and a backward propagating receiver wavefield coincide in time. RTM requires the simultaneous availability of source and receiver wavefields to perform wavefield matching through an imaging condition. Neglecting source motion effects in RTM can introduce artifacts in the final image or inaccuracies in phase and position of structures (Guitton et al., 2021).

In this paper, we present a solution to account for the source-motion effects in the seismic wavefield. We compute the wavefields required by RTM using the acoustic wave equation in a generalized coordinate system that takes into account source motion effects (Almuteri et al., 2022). Our approach uses coordinate transformations to map the physical domain tracking the moving source, to a regular fixed computational domain, enabling modeling wavefields triggered by moving sources. We demonstrate that such an approach produces accurate subsurface images as if the acquisition were conducted using stationary sources and thus

enabling the widespread use of marine vibrator sources for high-end techniques like reverse-time migration and full-waveform inversion.

2 THEORY

2.1 Tensorial acoustic wave equation

The acoustic wave equation in a generalized coordinate system defined by the variables $\boldsymbol{\xi} = \left[\xi^0, \xi^1, \xi^2, \xi^3\right]$ (Konuk and Shragge, 2020) is

$$\Box_\xi P_\xi = F_\xi, \tag{1}$$

where $\Box_\xi$ is the generalized d'Alembert operator, P_ξ is the pressure field, and F_ξ is the source function. The ξ^0 coordinate is time and $\left(\xi^1, \xi^2, \xi^3\right)$ are space components, and are related to a Cartesian physical domain defined by $\boldsymbol{x} = \left[x^0, x^1, x^2, x^3\right] = [t, x, y, z]$ through one-to-one mappings $\boldsymbol{x} = \boldsymbol{x}(\boldsymbol{\xi})$ and $\boldsymbol{\xi} = \boldsymbol{\xi}(\boldsymbol{x})$. The d'Alembert operator is

$$\Box_\xi = \frac{-1}{\sqrt{|\boldsymbol{g}|}} \frac{\partial}{\partial \xi^\mu} \left(\sqrt{|\boldsymbol{g}|} g^{\mu\nu} \frac{\partial}{\partial \xi^\nu} \right), \; \mu, \nu = 0, \cdots, 3, \tag{2}$$

where $[g^{\mu\nu}]$ is a contravariant metric tensor and $|\boldsymbol{g}|$ is its determinant. In a Cartesian coordinate system the d'Alembert operator (equation 2) is

$$\Box = \frac{-1}{c^2} \frac{\partial^2}{\partial t^2} + \nabla^2, \tag{3}$$

where $c(x, y, z)$ is the Cartesian medium velocity and ∇^2 is the Cartesian Laplacian operator. The contravariant metric tensor $[g^{\mu\nu}]$ is defined as the inverse of a covariant metric tensor $[g_{\mu\nu}]$ whose elements are

$$g_{\mu\nu} = \frac{\partial x^i}{\partial \xi^\mu} \frac{\partial x^i}{\partial \xi^\nu} \quad \text{for} \quad i, \mu, \nu = 0, \cdots, 3, \tag{4}$$

where repeated indices imply summation.

To model wavefields triggered by a moving source, we define a coordinate transformation that maps a horizontally deformed physical domain to a regular computational domain. To define such a coordinate transformation, we make assumptions that allow us to express the relationship between the $\boldsymbol{\xi}$- and $\boldsymbol{x}$-coordinate systems as

$$\begin{bmatrix} x^0 \\ x^1 \\ x^2 \\ x^3 \end{bmatrix} = \begin{bmatrix} \xi^0 \\ \xi^1 + v\xi^0 e^{\gamma(s_z - \xi^3)} \\ \xi^2 \\ \xi^3 \end{bmatrix}, \tag{5}$$

where v is the source velocity, γ is a user-defined decay factor that controls the amount of horizontal deformation as a function of depth, and s_z is the source depth. Therefore, the generalized d'Alembert operator (equation 2) for deformed source-tracking mesh along the ξ^1-axis reduces to a second-order AWE of the form

$$\frac{1}{T_1} \frac{\partial}{\partial \tau} \left(\frac{T_1}{c^2} \frac{\partial P_\xi}{\partial \tau} \right) = \frac{1}{T_1} \left[\frac{\partial}{\partial \xi^1} \left(\frac{T_0}{c} \frac{\partial P_\xi}{\partial \tau} \right) + \frac{\partial}{\partial \tau} \left(\frac{T_0}{c} \frac{\partial P_\xi}{\partial \xi^1} \right) \right] + \frac{1}{T_1} \frac{\partial}{\partial \xi^i} \left(T_1 g^{ij} \frac{\partial P_\xi}{\partial \xi^j} \right) + F_\xi, \tag{6}$$

where $T = \xi^1 + v\xi^0 e^{\gamma(s_z - \xi^3)}$, $T_k = \frac{\partial T}{\partial \xi^k}$, and $i, j = 1, 2, 3$ are spatial indices. We discuss the modeling approach in more detail in a companion report (Almuteri et al., 2022).

2.2 Reverse-time migration

We can define seismic data modeled in generalized coordinates due to a moving source as

$$\mathbf{d}_x = \mathbf{D}\mathbf{S}_x\mathbf{L}_\xi\mathbf{m}, \tag{7}$$

where $\mathbf{d}_x$ are the acquired data, $\mathbf{m}$ is an image (or estimated reflectivity) of the subsurface, $\mathbf{L}_\xi$ is the generalized demigration operator, $\mathbf{S}_x$ is a mapping operator from the generalized to the Cartesian coordinate system, and $\mathbf{D}$ is the data acquisition (or extractor) operator. For ocean-bottom acquisition and a judicious choice of the parameter γ (Almuteri et al., 2022), $\mathbf{D}\mathbf{S}_x \approx \mathbf{D}$ and no interpolation to Cartesian coordinates is required because the second term on the right-hand side of equation 5 will be negligible.

One can reconstruct a subsurface image using the adjoint operators $\mathbf{L}_\xi^T$ and $\mathbf{D}^T$ such that

$$\mathbf{m} = \mathbf{L}_\xi^T \mathbf{D}^T \mathbf{d}_x, \tag{8}$$

where $\mathbf{D}^T$ is an injector operator and $\mathbf{L}_\xi^T$ is the migration operator. The migration operator $\mathbf{L}_\xi^T$ backpropagates (processed) recorded data $\mathbf{d}_x$, computes the receiver wavefield $\mathbf{U}_r$, and applies an imaging condition that involves the source wavefield $\mathbf{U}_s$ given by

$$\mathbf{U}_s = \mathbf{S}_x \mathbf{L}_\xi \mathbf{m}. \tag{9}$$

Assuming ocean-bottom acquisition where receivers are stationary, one can compute the receiver wavefield using a Cartesian finite-difference acoustic wave-equation solver. In the case of ocean-bottom acquisition, and again with a judicious choice of γ, many terms in the generalized acoustic wave equation will be negligible (i.e., produces no significant wavefield contribution). Ignoring these terms reduces equation 6 to the Cartesian-based acoustic wave equation. Therefore, are only need to solve the acoustic wave equation in a generalized coordinate system to compute the source wavefield.

To construct an image of the subsurface, one needs to use an imaging condition to compare the source and receiver wavefields. A common imaging condition is the zero-lag cross-correlation. Such an imaging condition is suitable for data acquired using impulsive sources (e.g., air-guns). However, for non-impulsive sources with a long duration (e.g., marine vibrators), the zero-lag cross-correlation imaging condition produces images with strong artifacts. Alternatively, the deconvolution imaging condition is ideal for long sweeps. A frequency-domain deconvolution imaging condition is

$$\mathbf{m}(x,y,z) = \sum_e \sum_\omega \frac{\overline{\mathbf{U}}_s \mathbf{U}_r}{\overline{\mathbf{U}}_s \mathbf{U}_s + \epsilon}, \tag{10}$$

where $\overline{\mathbf{U}}_s(x,y,z,\omega)$ is the complex conjugate of $\mathbf{U}_s(x,y,z,\omega)$, ϵ is a stabilization factor to avoid division by zero, and summation is over different frequencies (ω) and experiments (e).

2.3 Adjoint modeling operator

Given our choice of coordinate transformation (equation 5), and assuming a slowly varying velocity, equation 6 reduces to

$$\frac{\partial^2 P_\xi}{\partial \tau^2} = 2cT_0 \frac{\partial}{\partial \xi^1}\left(\frac{\partial P_\xi}{\partial \tau}\right) + c^2 \frac{\partial}{\partial \xi^i}\left(g^{ij}\frac{\partial P_\xi}{\partial \xi^j}\right) + F_\xi, \tag{11}$$

where $i,j = 1,2,3$ are spatial indices. Discretizing equation 11 with respect to time using a second- and first-order approximations for the second- and first-order derivatives, respectively, results in

$$\frac{P_\xi^+ - 2P_\xi^0 + P_\xi^-}{\Delta\tau^2} = \frac{2cT_0}{\Delta\tau}\frac{\partial}{\partial\xi^1}\left(P_\xi^0 - P_\xi^-\right) + c^2\frac{\partial}{\partial\xi^i}\left(g^{ij}\frac{\partial P_\xi^0}{\partial\xi^j}\right) + F_\xi^0, \tag{12}$$

where P_ξ^+, P_ξ^0, and P_ξ^- indicate the wavefield at a future, current, and a previous time-step, respectively. To introduce operator notation, we re-order equation 12 to

$$\left(\frac{1}{\Delta\tau^2} + \frac{2cT_0}{\Delta\tau}\frac{\partial}{\partial\xi^1}\right)P_\xi^- - \left(\frac{2}{\Delta\tau^2} + \frac{2cT_0}{\Delta\tau}\frac{\partial}{\partial\xi^1} + \mathbf{H}\right)P_\xi^0 + \frac{1}{\Delta\tau^2}P_\xi^+ = F_\xi^0, \tag{13}$$

where $\mathbf{H} = c^2\frac{\partial}{\partial\xi^i}\left(g^{ij}\frac{\partial}{\partial\xi^j}\right)$. In matrix-vector notation, we can write equation 13 as

$$\begin{bmatrix} -\left(\frac{2}{\Delta\tau^2} + \frac{2cT_0}{\Delta\tau}\frac{\partial}{\partial\xi^1} + \mathbf{H}\right) & \frac{1}{\Delta\tau^2} & 0 & \cdots \\ \left(\frac{1}{\Delta\tau^2} + \frac{2cT_0}{\Delta\tau}\frac{\partial}{\partial\xi^1}\right) & -\left(\frac{2}{\Delta\tau^2} + \frac{2cT_0}{\Delta\tau}\frac{\partial}{\partial\xi^1} + \mathbf{H}\right) & \frac{1}{\Delta\tau^2} & \cdots \\ 0 & \left(\frac{1}{\Delta\tau^2} + \frac{2cT_0}{\Delta\tau}\frac{\partial}{\partial\xi^1}\right) & -\left(\frac{2}{\Delta\tau^2} + \frac{2cT_0}{\Delta\tau}\frac{\partial}{\partial\xi^1} + \mathbf{H}\right) & \cdots \\ \vdots & \vdots & \vdots & \ddots \end{bmatrix} \begin{bmatrix} P_\xi^0 \\ P_\xi^1 \\ P_\xi^2 \\ \vdots \end{bmatrix} = \begin{bmatrix} F_\xi^0 \\ F_\xi^1 \\ F_\xi^2 \\ \vdots \end{bmatrix}, \tag{14}$$

which we can write in a compact form as

$$\mathbf{W}\mathbf{P}_\xi = \mathbf{F}_\xi. \tag{15}$$

Therefore, the adjoint equation has the equivalent matrix form

$$\mathbf{W}^T\mathbf{F}_\xi = \mathbf{P}_\xi, \tag{16}$$

which expands to

$$\begin{bmatrix} -\left(\frac{2}{\Delta\tau^2}+\frac{2}{\Delta\tau}\frac{\partial}{\partial\xi^1}cT_0+\mathbf{H}^T\right) & \left(\frac{1}{\Delta\tau^2}+\frac{2}{\Delta\tau}\frac{\partial}{\partial\xi^1}cT_0\right) & 0 & \cdots \\ \frac{1}{\Delta\tau^2} & -\left(\frac{2}{\Delta\tau^2}+\frac{2}{\Delta\tau}\frac{\partial}{\partial\xi^1}cT_0+\mathbf{H}^T\right) & \left(\frac{1}{\Delta\tau^2}+\frac{2}{\Delta\tau}\frac{\partial}{\partial\xi^1}cT_0\right) & \cdots \\ 0 & \frac{1}{\Delta\tau^2} & -\left(\frac{2}{\Delta\tau^2}+\frac{2}{\Delta\tau}\frac{\partial}{\partial\xi^1}cT_0+\mathbf{H}^T\right) & \cdots \\ \vdots & \vdots & \vdots & \ddots \end{bmatrix} \begin{bmatrix} F_\xi^0 \\ F_\xi^1 \\ F_\xi^2 \\ \vdots \end{bmatrix} = \begin{bmatrix} P_\xi^0 \\ P_\xi^1 \\ P_\xi^2 \\ \vdots \end{bmatrix}, \tag{17}$$

where $\mathbf{H}^T = \frac{\partial}{\partial\xi^j}\left(g^{ij}\frac{\partial}{\partial\xi^i}c^2\right)$. Equation 17 can be re-written in a similar format to equation 13 as

$$\frac{1}{\Delta\tau^2}F_\xi^- - \left(\frac{2}{\Delta\tau^2}+\frac{2}{\Delta\tau}\frac{\partial}{\partial\xi^1}cT_0+\mathbf{H}^T\right)F_\xi^0 + \left(\frac{1}{\Delta\tau^2}+\frac{2}{\Delta\tau}\frac{\partial}{\partial\xi^1}cT_0\right)F_\xi^+ = P_\xi^0. \tag{18}$$

We can respectively write equations 13 and 18 in a time recursion representation as

$$P_\xi^+ = \Delta\tau^2 F_\xi^0 + \Delta\tau^2\left(\frac{2}{\Delta\tau^2}+\frac{2cT_0}{\Delta\tau}\frac{\partial}{\partial\xi^1}+\mathbf{H}\right)P_\xi^0 - \Delta\tau^2\left(\frac{1}{\Delta\tau^2}+\frac{2cT_0}{\Delta\tau}\frac{\partial}{\partial\xi^1}\right)P_\xi^-, \tag{19}$$

and

$$F_\xi^- = \Delta\tau^2 P_\xi^0 + \Delta\tau^2\left(\frac{2}{\Delta\tau^2}+\frac{2}{\Delta\tau}\frac{\partial}{\partial\xi^1}cT_0+\mathbf{H}^T\right)F_\xi^0 - \Delta\tau^2\left(\frac{1}{\Delta\tau^2}+\frac{2}{\Delta\tau}\frac{\partial}{\partial\xi^1}cT_0\right)F_\xi^+. \tag{20}$$

The forward and adjoint time recursion equations (equations 19 and 20) show that the receiver wavefield computed by a simple time reversal is not equivalent to the adjoint wavefield, although the time-stepping solutions are similar for the forward and adjoint operation formulated forward and backward in time, respectively. In ocean-bottom acquisition, one can compute the receiver wavefield using the adjoint of the Cartesian-based acoustic wave equation for simplification because receivers are stationary, although using equation 20 is the appropriate approach. This simplification is not applicable when using our imaging procedure on streamer data because receivers are in continuous motion.

3 NUMERICAL EXAMPLES

3.1 Scattering points model

To illustrate the effectiveness of our imaging approach, we first use a constant velocity model with five vertically-aligned scattering points to simulate two synthetic datasets: with and without moving sources. We simulate datasets using 41 sources at $s_z = 12.5$ m with a 32.5 m source-initiation interval spacing. Also, we use 237 receivers at depth $x^3 = 375$ m with a 6.25 m receiver spacing. We model data for 2.0 s with a temporal sampling interval of 0.5 ms. For the moving source acquisition, we use a source boat velocity of 25 m/s, which is high comparing to the typical $2-3$ m/s of conventional marine acquisition; however, this allows us to highlight the significance of source motion on seismic imaging as well as the ability of our method to accurately image the subsurface. The source function is a linear sweep from 22 Hz to 41 Hz.

Figures 1a-1c show RTM images generated using stationary sources acquisition and imaging, moving sources acquisition and stationary imaging, and moving sources acquisition and imaging, respectively. Here, we consider the case of stationary sources acquisition and imaging as the reference scenario. Ignoring the source-motion effects results in a distorted image of the scattering points, introducing asymmetry that is not present in the reference image (Figure 1d), and appears as false structures. Such asymmetry could falsely imply imbalanced illumination, a velocity model error, or a combination of both. Further, the distortion in the scattering points lessen with depth, showing that source motion effects are more significant for shallow targets than deep targets.

Taking into consideration the source motion when computing the source wavefield (i.e., using a moving imaging procedure) produces an image that closely matches the one obtained from a stationary acquisition (Figure 1e). However, the two images (Figures 1a and 1c) are not identical for two reasons. First, the source wavefield is influenced by the Doppler effect due to the source motion, whereas the receiver wavefield is free of such effects because the receivers are stationary. In such a situation, the source and receiver wavefields have different observed frequencies except at scattering point locations. Second, the recorded data are different between the two acquisitions (e.g., different amplitude-versus-angle for different frequencies) and different portions of the wavefield are recorded by the two acquisitions.

Figures 2a-2c show common image gathers (CIG) generated using stationary sources acquisition and imaging, moving sources acquisition and stationary imaging, and moving sources acquisition and imaging, respectively, for the surface location $x^1 = 750$ m. The CIGs show that all events horizontally align for the stationary sources acquisition and imaging (Figure 2a), and for the moving sources acquisition and imaging (Figure 2c). However, for the moving sources acquisition and stationary imaging, the CIG (Figure

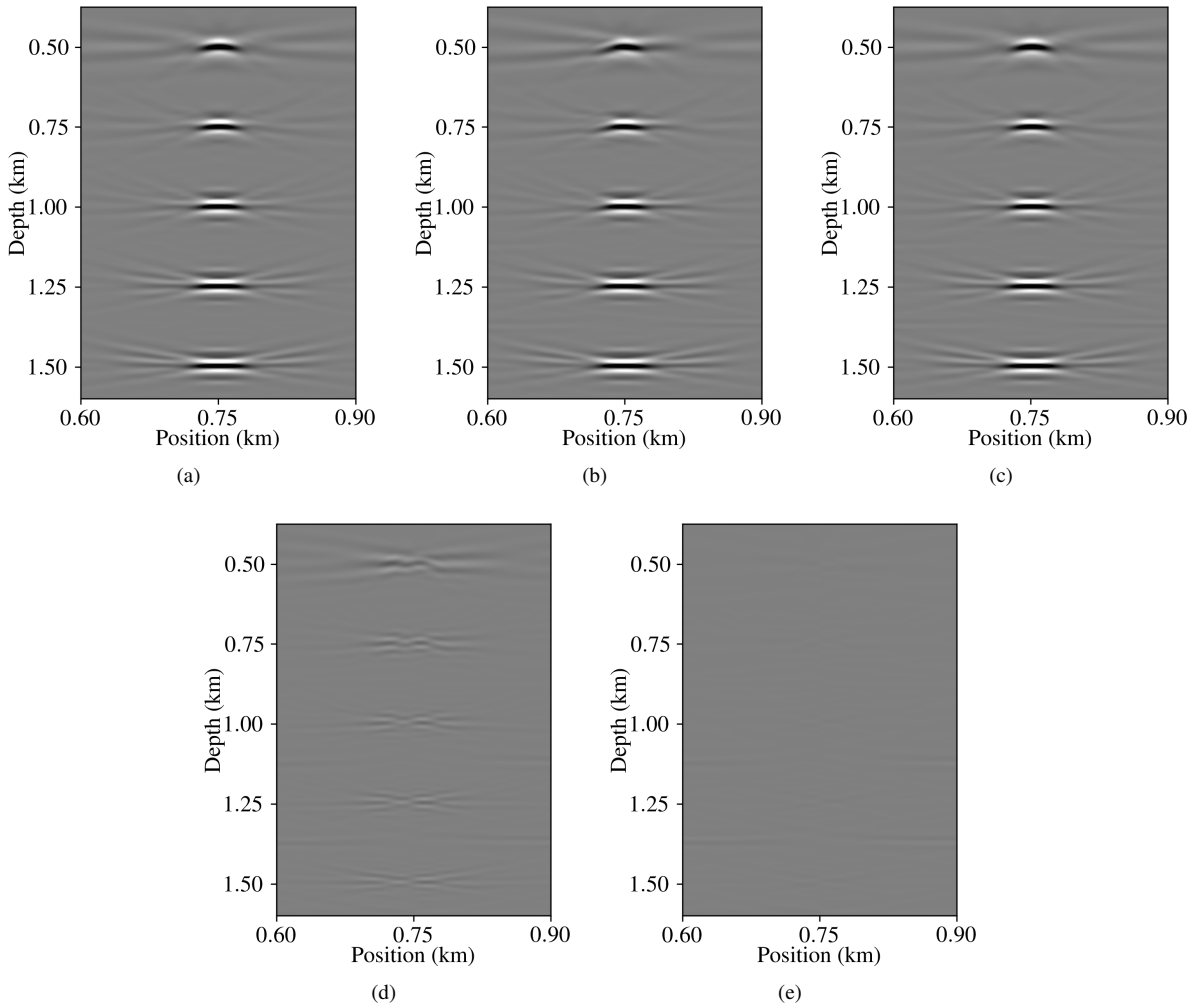

Figure 1. RTM image of the scattering points model computed using (a) stationary sources and imaging, (b) mobile sources and stationary imaging, and (c) mobile sources and moving imaging. Difference between the images shown in (d) Figures 1(a) and 1(b), and (e) Figures 1(a) and 1(c).

2b) shows that the events are slightly dipping with a maximum dip for the shallowest event (at $x^3 = 500$ m) and minimum dip for the deepest event ($x^3 = 1500$ m), highlighting the significance of source motion effects on shallow targets.

3.2 Marmousi II model

To examine our approach in a more complex scenario, we use a section of the Marmousi II model. In this experiment, we simulate datasets using 47 sources at $s_z = 12.5$ m with a 50 m source-initiation interval spacing. Also, we use 199 receivers at depth $x^3 = 375$ m with a 12.5 m receiver spacing. We model data for 2.5 s with a temporal sampling interval of 0.5 ms. Figures 3a-3c respectively show the RTM images generated using stationary sources acquisition and imaging, moving sources acquisition and stationary imaging, and moving sources acquisition and imaging. At first glance all images look similar; however, the difference between stationary acquisition and imaging and mobile sources acquisition and stationary imaging (Figure 3d) shows a phase change and mispositioning of imaged structures. This observation is consistent with that of Guitton et al. (2021), which reports similar results. However, taking source motion effects into account using the approach developed here produces a subsurface image very similar to that from the stationary acquisition scenario (Figure 3e).

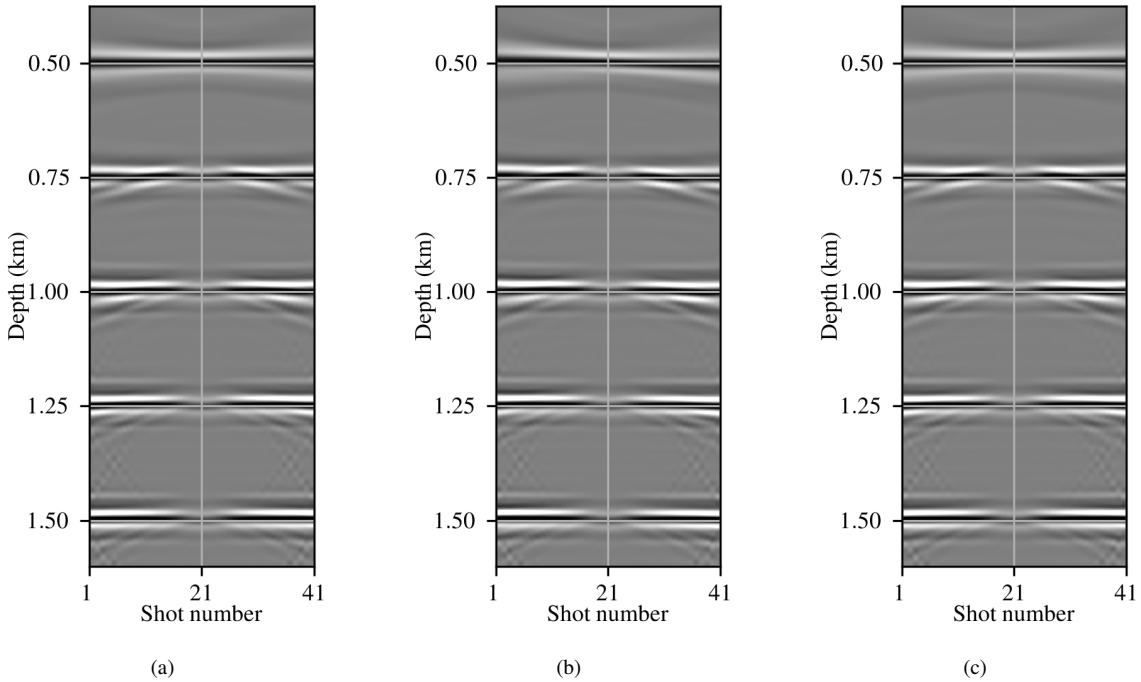

Figure 2. CIGs of the scattering points model computed using (a) stationary sources and imaging, (b) mobile sources and stationary imaging, and (c) mobile sources and moving imaging, for the surface location $x^1 = 750$ m.

4 DISCUSSION

As may be expected, neglecting the Doppler effects and the time-dependent source-receiver offsets in RTM produces distorted subsurface images. Here, we present an RTM framework for subsurface imaging using marine vibrator data that accounts for the mobile acquisition. The developed approach utilizes a coordinate transformation to compute the required source and receiver wavefields used to evaluate the deconvolution imaging condition. Further, for a judicious choice of grid parameters in ocean-bottom acquisition, one can compute the receiver wavefield using a Cartesian finite-differences acoustic wave-equation solver. The resulting examples demonstrate that the proposed method can accurately image the subsurface even with unrealistically high motion of the mobile marine vibrator source.

The results show that source motion effects are more significant for shallow targets than deep targets because the source motion relative to the shallow targets is greater. Further, the observed frequencies, i.e. the Doppler effect, at a receiver location for a scattered wavefield is independent of the source-receiver relative locations. Frequency shifts observed at a receiver location are controlled by the source velocity and the scattering point location relative to the source (Almuteri et al., 2022). Further, source motion complicates velocity model building because neglecting source motion effects makes velocity model building prone to errors, especially for shallow sections.

5 CONCLUSIONS

This work presents an RTM imaging solution for mobile marine acquisition without a need for shot or receiver interpolation. Further, our approach does not require a specialized processing workflow to remove the source motion from the acquired data; the approach inherently accounts for source motion effects by a judicious choice of coordinate transformation that uses the actual source velocity. There is an added computational cost to account for the source motion effects in the acoustic wave equation, thus ensuring accurate and robust modeling and imaging of marine vibrator data. In streamer data acquisition, even though air-guns are instantaneous, streamers are in continuous motion. Such motion introduces the Doppler effect to the data. Therefore, our proposed method is not limited to marine vibrator data, but can also be used to image moving streamer data. Future work involves incorporating a dynamic sea surface to mimic more realistic marine vibrator acquisition scenarios.

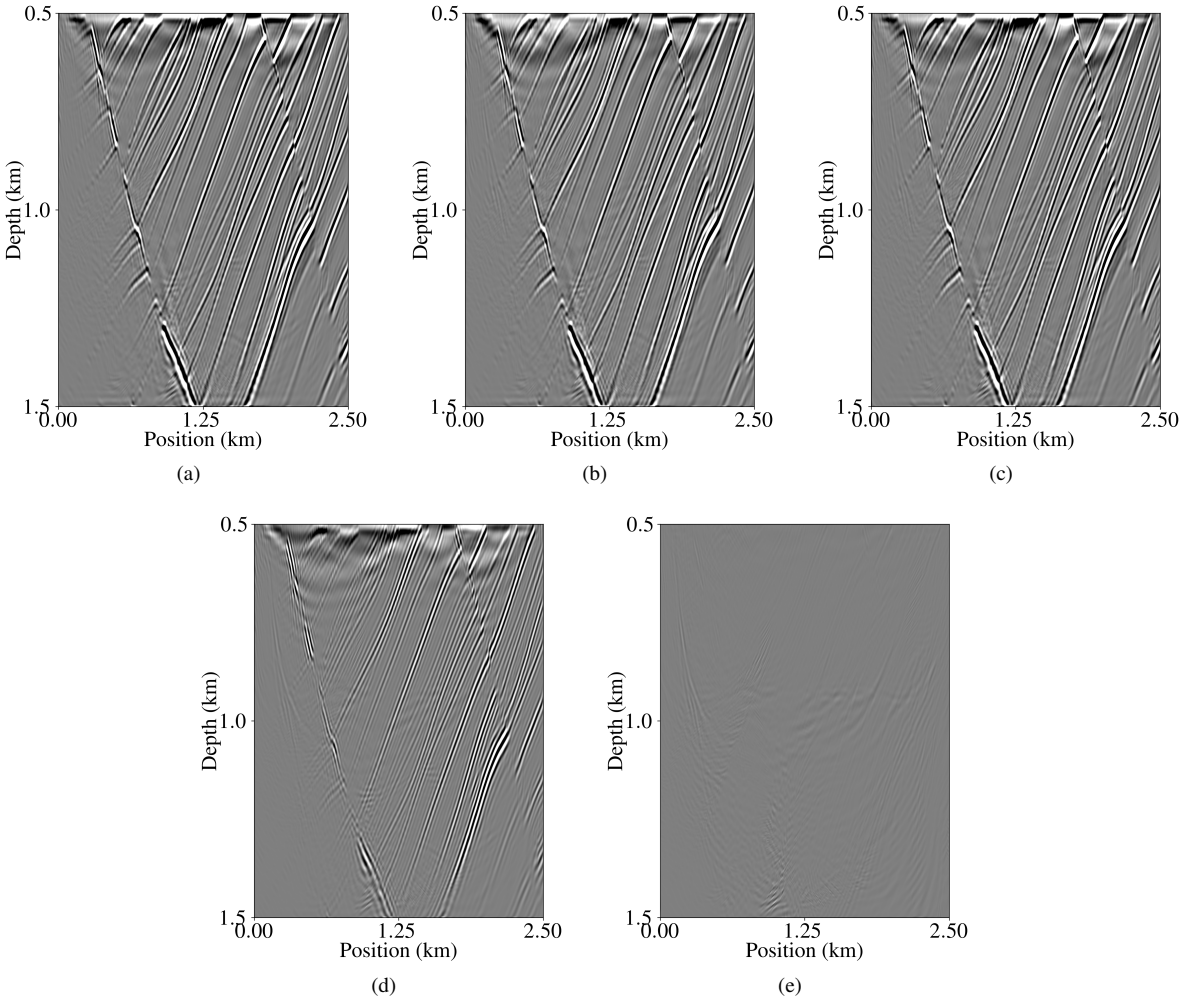

Figure 3. RTM image of the Marmousi II sub-model computed using (a) stationary sources and imaging, (b) mobile sources and stationary imaging, and (c) mobile sources and imaging. Difference between the images shown in (d) Figures 3(a) and 3(b), and (e) Figures 3(a) and 3(c).

6 ACKNOWLEDGEMENTS

The first author would like to thank Saudi Aramco for graduate study sponsorship. We thank the sponsors of the Center for Wave Phenomena consortium at the Colorado School of Mines for the support of this research. We also thank Antoine Guitton from Total Energies for helpful discussions.

REFERENCES

Almuteri, K., J. Shragge, and P. Sava, 2022, Finite-difference modeling of marine vibrator sources: CWP report, **1001**.

Baysal, E., D. D. Kosloff, and J. W. Sherwood, 1983, Reverse time migration: Geophysics, **48**, no. 11, 1514–1524. (doi:https://dx.doi.org/https://doi.org/10.1190/1.1441434).

Claerbout, J. F., 1971, Toward a unified theory of reflector mapping: Geophysics, **36**, no. 3, 467–481. (doi:https://dx.doi.org/10.1190/1.1440185).

Guitton, A., B. Duquet, S. Secker, J.-P. Mascomere, and A. Feltham, 2021, A deconvolution-interpolation approach with sparse inversion to mitigate the Doppler effect in marine vibrators data: First International Meeting for Applied Geoscience & Energy, Society of Exploration Geophysicists, 2555–2559. (doi:https://dx.doi.org/10.1190/segam2021-3593897.1).

Konuk, T., and J. Shragge, 2020, Modeling full-wavefield time-varying sea-surface effects on seismic data: A mimetic finite-difference approach: Geophysics, **85**, no. 2, T45–T55. (doi:https://dx.doi.org/10.1190/geo2019-0181.1).

Laws, R., D. Halliday, J.-F. Hopperstad, D. Gerez, M. Supawala, A. Özbek, T. Murray, and E. Kragh, 2019, Marine vibrators: the new phase of seismic exploration: Geophysical Prospecting, **67**, no. 6, 1443–1471. (doi:https://dx.doi.org/10.1111/1365-2478.12708).

McMechan, G. A., 1983, Migration by extrapolation of time-dependent boundary values: Geophysical Prospecting, **31**, no. 3, 413–420. (doi:https://dx.doi.org/10.1111/j.1365-2478.1983.tb01060.x).

Wason, H., and F. J. Herrmann, 2013, Time-jittered ocean bottom seismic acquisition, *in* 83rd Annual International Meeting: SEG, Expanded Abstracts. (doi:https://dx.doi.org/10.1190/segam2013-1391.1).

Whitmore, N. D., 1983, Iterative depth migration by backward time propagation: 53rd Annual International Meeting, SEG, Expanded Abstracts, 382–385. (doi:https://dx.doi.org/10.1190/1.1893867).